A&A 660, A64 (2022)
https://doi.org/10.1051/0004-6361/202140954

Astronomy & Astrophysics
Special issue

Solar Orbiter First Results (Cruise Phase)

Analysis of multiscale structures at the quasi-perpendicular Venus bow shock

Results from Solar Orbiter's first Venus flyby

A. P. Dimmock[1], Yu. V. Khotyaintsev[1], A. Lalti[1,2], E. Yordanova[1], N. J. T. Edberg[1], K. Steinvall[1,2], D. B. Graham[1], L. Z. Hadid[3], R. C. Allen[4], A. Vaivads[5], M. Maksimovic[6], S. D. Bale[7,8], T. Chust[3], V. Krasnoselskikh[9,7], M. Kretzschmar[9,10], E. Lorfèvre[11], D. Plettemeier[12], J. Souček[13], M. Steller[14], Š. Štverák[13,15], P. Trávníček[7,15], A. Vecchio[6,16], T. S. Horbury[17], H. O'Brien[17], V. Evans[17], and V. Angelini[17]

[1] Swedish Institute of Space Physics (IRF), Uppsala, Sweden
e-mail: andrew.dimmock@irfu.se
[2] Space and Plasma Physics, Department of Physics and Astronomy, Uppsala University, Uppsala 75120, Sweden
[3] LPP, CNRS, Ecole Polytechnique, Sorbonne Université, Observatoire de Paris, Université Paris-Saclay, Palaiseau, Paris, France
[4] Johns Hopkins Applied Physics Lab, Laurel, MD 20723, USA
[5] Division of Space and Plasma Physics, School of Electrical Engineering and Computer Science, KTH Royal Institute of Technology, Stockholm 11428, Sweden
[6] LESIA, Observatoire de Paris, Université PSL, CNRS, Sorbonne Université, Univ. Paris Diderot, Sorbonne Paris Cité, 5 Place Jules Janssen, 92195 Meudon, France
[7] Space Sciences Laboratory, University of California, Berkeley, CA, USA
[8] Physics Department, University of California, Berkeley, CA, USA
[9] LPC2E, CNRS, 3A avenue de la Recherche Scientifique, Orléans, France
[10] Université d'Orléans, Orléans, France
[11] CNES, 18 Avenue Edouard Belin, 31400 Toulouse, France
[12] Technische Universität Dresden, Helmholtz Str. 10, 01187 Dresden, Germany
[13] Institute of Atmospheric Physics of the Czech Academy of Sciences, Prague, Czech Republic
[14] Space Research Institute, Austrian Academy of Sciences, Graz, Austria
[15] Astronomical Institute of the Czech Academy of Sciences, Prague, Czech Republic
[16] Radboud Radio Lab, Department of Astrophysics, Radboud University, Nijmegen, The Netherlands
[17] Imperial College London, South Kensington Campus, London SW7 2AZ, UK

Received 31 March 2021 / Accepted 1 February 2022

ABSTRACT

Context. Solar Orbiter is a European Space Agency mission with a suite of in situ and remote sensing instruments to investigate the physical processes across the inner heliosphere. During the mission, the spacecraft is expected to perform multiple Venus gravity assist maneuvers while providing measurements of the Venusian plasma environment. The first of these occurred on 27 December 2020, in which the spacecraft measured the regions such as the distant and near Venus magnetotail, magnetosheath, and bow shock.
Aims. This study aims to investigate the outbound Venus bow shock crossing measured by Solar Orbiter during the first flyby. We study the complex features of the bow shock traversal in which multiple large amplitude magnetic field and density structures were observed as well as higher frequency waves. Our aim is to understand the physical mechanisms responsible for these high amplitude structures, characterize the higher frequency waves, determine the source of the waves, and put these results into context with terrestrial bow shock observations.
Methods. High cadence magnetic field, electric field, and electron density measurements were employed to characterize the properties of the large amplitude structures and identify the relevant physical process. Minimum variance analysis, theoretical shock descriptions, coherency analysis, and singular value decomposition were used to study the properties of the higher frequency waves to compare and identify the wave mode.
Results. The non-planar features of the bow shock are consistent with shock rippling and/or large amplitude whistler waves. Higher frequency waves are identified as whistler-mode waves, but their properties across the shock imply they may be generated by electron beams and temperature anisotropies.
Conclusions. The Venus bow shock at a moderately high Mach number (~5) in the quasi-perpendicular regime exhibits complex features similar to the Earth's bow shock at comparable Mach numbers. The study highlights the need to be able to distinguish between large amplitude waves and spatial structures such as shock rippling. The simultaneous high frequency observations also demonstrate the complex nature of energy dissipation at the shock and the important question of understanding cross-scale coupling in these complex regions. These observations will be important to interpreting future planetary missions and additional gravity assist maneuvers.

Key words. shock waves – plasmas – waves – instabilities – polarization

1. Introduction

Although Venus is of a comparable size and composition to Earth, decades of observations have confirmed that Venus lacks any significant intrinsic magnetic field (Phillips & Russell 1987). As a result, the obstacle presented to the solar wind is the highly conducting ionosphere (Luhmann 1986), in which draping of the interplanetary magnetic field (IMF) lines around it forms an induced magnetosphere. This presents some similarities to Earth (e.g., bow shock, magnetosheath, magnetotail), albeit with some fundamental differences such as a decreased bow shock stand-off distance (1–2 R_V), which is significantly closer than Earth (12 R_E), considering that $R_E \sim R_V \sim 6500$ km. Examining the solar wind-Venus interaction not only advances our understanding of the plasma environment around unmagnetized bodies, but it is also highly beneficial to understanding universal plasma processes such as collisionless shocks, turbulence, particle energization, and heating.

The Solar Orbiter (SolO) mission (Müller et al. 2020) is expected to perform several Venus gravity assist maneuvers (VGAMs); the first (VGAM1) of these occurred on 27 December 2020, which is the focus of this study. SolO offers significantly higher resolution measurements compared to previous Venus missions (e.g., Venus Express and Pioneer Venus Orbiter), which are ideal for probing the complex small scale structures and multiscale electromagnetic waves reported at the bow shock. Unexpectedly, SolO did not observe the well-defined classical quasi-perpendicular shock profile of a foot, ramp, and overshoot, but instead, the shock crossing was populated with numerous magnetic field and density structures as well as electromagnetic waves. These measurements are of high scientific importance since previously dedicated Venus missions could not have captured them, thus revealing new insights into the behavior of the Venusian bow shock. This paper analyzes these rare observations in detail, providing physical interpretations and putting the observations in context with current knowledge of heliospheric collisionless shocks.

The main function of a collisionless shock is to redistribute the kinetic energy contained in the supermagnetosonic bulk flow into other degrees of freedom, such as particle heating and acceleration (Kennel et al. 1985). Although the manner that this is achieved depends on many parameters, two of these are highly critical. First is the shock geometry, which is defined as quasi-parallel or quasi-perpendicular if the angle between the shock surface normal ($\hat{\boldsymbol{n}}$) and upstream magnetic field ($\mathbf{B}_u$) is <45° or >45°, respectively. Second is the Alfvén Mach number (M_A), which is the ratio between the upstream velocity ($\mathbf{V}_{us}$) along $\hat{\boldsymbol{n}}$ and the Alfvén speed (V_A). Depending on the value of M_A, numerous energy dissipation mechanisms take place to balance the nonlinear steepening of the shock ramp (Kennel et al. 1985), which manifests in the global magnetic shock profile and the array of complex multiscale structures that can develop close to the shock front. For example, the large scale structure of the shock front can be modified by processes such as nonstationarity (Krasnoselskikh et al. 2002) and rippling (Johlander et al. 2016), whereas even smaller scale variations such as whistler waves are frequently observed and play a key role in energy dissipation (Balikhin et al. 1997).

Typically, the magnetic profile of a super-critical quasi-perpendicular shock consists of well-defined foot, ramp, and overshoot regions. The foot is located immediately upstream of the ramp and is formed due to the gyration of reflected ions, the ramp is the region of the steepest magnetic gradient, and the overshoot manifests as downstream oscillations due to the gyrophase mixing of plasma shortly downstream. This classical shock profile has been challenged by high-resolution measurements for many years due to the existence of an array of complex multiscale structures (see Bale et al. 2005 and references therein) that are observed in many conditions. This study contributes to understanding this non-classical shock profile not just at Earth, but Venus as well. These structures are intrinsically associated with energy dissipation and will strongly depend on the shock Mach number (Kennel et al. 1985). Various physical mechanisms have been proposed to explain shock substructures such as the corrugation instability, shock front nonstationarity, large amplitude whistler waves, and shock rippling. Upstream variations can also have an impact, for example low-frequency shock rippling can be due to upstream magnetic turbulence that can manifest over extensive temporal and spatial scales (Pitňa et al. 2021; Zank et al. 2021). Nevertheless, many open questions remain.

Shock front nonstationarity is a regime when the physical dissipation mechanisms are no longer sufficient to counterbalance the nonlinear steepening of the shock ramp (Krasnoselskikh et al. 2002). This can eventually lead to a cyclic large scale magnetic reconfiguration of the shock profile (Morse et al. 1972; Krasnoselskikh 1985). One physical description of shock front nonstationarity is the gradient catastrophe model (Krasnoselskikh et al. 2002) that is initiated when the shock Mach number surpasses the whistler critical Mach number and whistlers can no longer propagate upstream. A key feature of the gradient catastrophe model is the manifestation of electron scale whistler structures within the ramp corresponding to the electron scale limit of the whistler branch. Recently, Dimmock et al. (2019) provided direct observational evidence of the gradient catastrophe model at the Earth's bow shock. This mechanism can offer a physical explanation for magnetic field structures resembling whistler waves in the shock front at higher Mach numbers.

Shock ripples can manifest across a range of length scales (Ofman & Gedalin 2013). They develop in simulations (Winske & Quest 1988; Lowe & Burgess 2003), and have been proposed through indirect observations (Lobzin et al. 2008). Winske & Quest (1988) proposed that the ion pressure anisotropy was responsible for shock ripples with lengths around six ion inertial lengths. Smaller scale ripples (Lowe & Burgess 2003) have also been attributed to instabilities; however, in this case, ion reflection was proposed as the cause, which was later supported by observations (Lobzin et al. 2008). Also, much larger ripples have been reported in simulations (Yuan et al. 2009) on the order of 30 ion inertial lengths.

The Magnetospheric Multiscale (MMS) mission has shed new light on shock rippling using a suite of instruments capable of delivering high cadence plasma measurements and resolving the spatial scales of the ripples. Using MMS data, Johlander et al. (2016) classified a rippled quasi-perpendicular shock based on phase-space holes in the ion phase-space density and corresponding variations in the magnetic field. Later, Johlander et al. (2018) performed a more detailed study based on a partial bow shock crossing where $\theta_{bn} = 64°$ and $M_A = 7$, which exhibited numerous and clear ripples. These observations demonstrated that magnetic field variations are accompanied by changes in electron density, and the ripples are linearly polarized, propagating in the coplanarity plane.

Low frequency (10^0–10^1 Hz) whistler waves are frequently observed near supercritical quasi-perpendicular shocks across multiple plasma environments (Fairfield 1974; Russell 2007; Wilson 2012; Dimmock et al. 2013; Wilson 2017) and are

crucial in dissipating energy. It is understood that in general, they arise due to either shock macro-dynamics (Krasnoselskikh 1985) or various instabilities (Wu et al. 1984). In some cases, these have been reported to reach high amplitudes approaching the shock amplitude, for example, Wilson (2012) studied large amplitude whistler waves at supercritical interplanetary shocks using Wind data. Interestingly, the authors calculated that their peak-peak amplitudes can reach almost twice the background magnetic field. In addition, they were not phase standing, had wave vector normal directions oblique to the background field and shock normal, exhibited right-handed circular polarization in the spacecraft reference frame, and had wave periods higher than the ion gyrofrequency in the plasma rest frame.

In addition to lower frequency precursors, higher frequency (30–120 Hz) whistler waves (with smaller amplitudes) have been observed near the foot and the ramp of supercritical quasi-perpendicular shocks (Zhang et al. 1999; Hull et al. 2020), which are also believed to play a key role in dissipating energy at the shock front. Such waves tend to propagate at small angles with respect to the background magnetic field (θ_{kb}) and are directed preferentially to the upstream direction. The high frequency whistler waves are the result of electron instabilities such as the electron beam instability (Tokar et al. 1984) or the temperature anisotropy ($Te_{\perp} > Te_{\parallel}$) instability (Hull et al. 2012). It has also been suggested that low and high frequency whistler waves may be coupled via the generation of currents in the shock layer (Hull et al. 2020), which may also be connected to electrostatic features in the shock front.

Although the non-laminar structure of non-terrestrial bow shocks via mechanisms such as shock nonstationarity, reformation, and rippling has been reported (Sundberg et al. 2013; Sulaiman et al. 2015), studies of this nature are still limited, likely owing to the constraints imposed by single spacecraft observations, typically lower cadence measurements, and the complexity of interpreting shock structures. To address this, we used the recent high-resolution magnetic field, electric field, and electron density measurements by SolO to investigate the shock structure at Venus with interpretations based on recent results (Johlander et al. 2018; Dimmock et al. 2019). The comparable Mach number regime of the Venus bow shock to Earth allows a valid comparison and can greatly help to interpret single spacecraft measurements that often have limited and/or lower resolution measurements. We also employed these measurements to analyze smaller scale wave modes that occur in concert with the larger scale shock front substructures. These results give new insights into interpreting challenging single-point measurements of planetary bow shocks, which are vital to understanding the behavior of collisionless shocks across different parameter spaces (e.g., spatial extent and Mach number).

2. Datasets and instrumentation

On 27 December 2020, SolO completed its first Venus gravity assist maneuver as illustrated in Fig. 1, which shows the SolO trajectory and fundamental model boundaries. The spacecraft approached the Venus plasma environment through the distant magnetotail at a distance of over $-80\,R_V$ from 01:50 UTC. From henceforth, all quoted times will be in UTC (universally coordinated time). The spacecraft continued traveling sunward toward the planet for almost 11 h before crossing the bow shock into the solar wind at approximately 12:40.

The present study utilized SolO observations around the outbound bow shock crossing between 12:39 and 12:41 at a location of $R_{\rm bs}$ =[0.1, −0.4, 2.2] R_V in VSO (Venus Solar Orbital) coordinates. In this study, we employed measurements from the Radio and Plasma Wave (RPW) and magnetometer (MAG) instruments, which captured interesting multiscale structures across the shock, which were analyzed in detail here. While the Energetic Particle Detector (EPD) (Rodríguez-Pacheco et al. 2020) was operating during the majority of VGAM1 (see Allen et al. 2021), several of the EPD sensors were briefly turned off near the closest approach due to the possibility of light contamination (see Wimmer-Schweingruber et al. 2021). Allen et al. (2021) provides an overview of EPD observations investigating acceleration processes around Venus; however, there were no reliable energetic particle measurements for this bow shock crossing and thus are not included in this study. Complete overviews of the RPW and MAG observations across the entire Venus flyby are also reported by Hadid et al. (2021) and Volwerk et al. (2021). Unfortunately, the Solar Wind Plasma Analyser (SWA) (Owen et al. 2020) was not operating during the Venus encounter. As a result of this, we have strictly focused on analyzing the interesting features in the magnetic field, electric field, and electron density, which are capable of diagnosing key shock phenomena such as rippling, reformation, and the properties of electromagnetic waves.

Fluxgate Magnetometer (FGM) (Horbury et al. 2020) observations from the MAG instrument (128 Hz) were employed to study the shock front profile and shock substructures. Search Coil Magnetometer (SCM) data (Jannet et al. 2021) and AC electric field (both at 256 Hz) from RPW were used to identify and characterize the features of whistler waves during the shock transition. The SCM measures the full 3D vector of magnetic fluctuations, while only two components of the AC electric field are available. This is because the AC electric field is measured by three antennas in the plane perpendicular to the radial direction from the Sun (see Fig. 7 in Maksimovic et al. 2020), leaving the radial electric field component unmeasured. The SCM, AC electric field, and spacecraft potential are all part of RWP instrument described in detail by Maksimovic et al. (2020). The spacecraft potential is proportional to the electron density in the ambient plasma, and also to the square root of the electron temperature. By calibrating the spacecraft potential to the absolute value of the density obtained from the detection of the plasma frequency line, which is obtained at a lower cadence, a high cadence (256 Hz) plasma density estimate is acquired (Khotyaintsev et al. 2021). This assumes that the temperature does not change significantly in-between the plasma frequency line detections. The electron density is used to characterize the shock substructures and compare them with the magnetic shock profile. It is also possible to derive the electron temperature from the thermal noise spectra; however, this has not been attempted yet for SolO. Nevertheless, the spectra is not available at the sufficient cadence to resolve the shock substructures that are the focus of this study.

3. Results: Analysis of the Venus bow shock

3.1. Determination of bow shock parameters

Accurate determination of the bow shock normal is critical to interpreting the features of collisionless shocks. This calculation is often not straightforward due to the presence of spatial and temporal variations within the shock front and/or the lack of multipoint measurements. The shock crossing that we examined contained large amplitude magnetic structures, which creates local changes in the shock normal. For this reason, we adopted the bow shock model of Martinecz et al. (2009), which provided

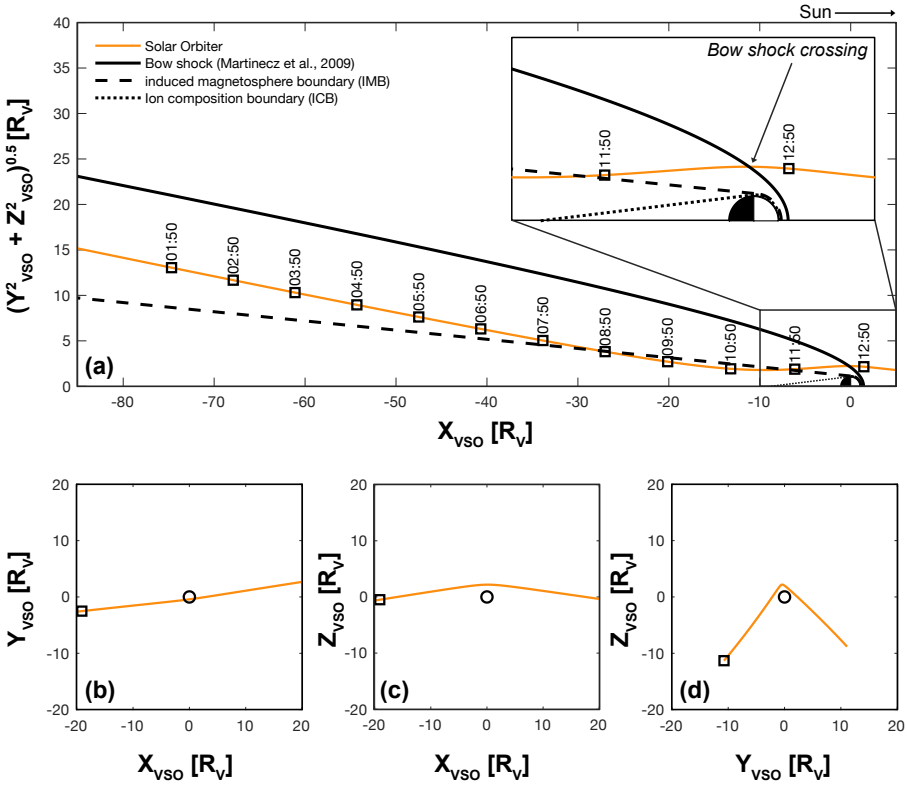

Fig. 1. Trajectory of VGAM1 in VSO coordinates. The spacecraft entered the Venus plasma environment in the far tail before crossing the bow shock around 12:40 close to the terminator.

a shock normal direction of $\hat{\boldsymbol{n}}$ = [0.58, −0.16, 0.80] and can be considered a global normal direction. This normal appears logical considering the location of the crossing is at the XZ terminator. In addition, from the model fitted data (see Martinecz et al. 2009), we would not expect substantial variations in the shock position that would significantly change this normal direction. The average upstream magnetic field $\mathbf{B_u}$ = [−3.0, 7.3, 4.0] nT resulted in a shock geometry of θ_{bn} = 89°. To increase confidence in this model normal, we also compared the minimum variance direction between 12:39:47.37 and 12:39:49.31. This period appears to be the final stage of the shock ramp and therefore the minimum variance direction of this interval should be closely aligned with the model normal. We identified the shock ramp as the final increase of the magnetic field and density before the downstream Venus magnetosheath. The magnetosheath is clear as the data shows the expected steady and enhanced magnetic field and density. As expected, the ramp gave a normal direction that differed by a small angle (∼9°) to the model normal. Yet, this direction was poorly defined ($\lambda_2/\lambda_3 < 10$) so henceforth we used the model normal direction. Further evidence in favor of the chosen $\hat{\boldsymbol{n}}$ can also be found by the negligible offset of $\mathbf{B} \cdot \hat{\boldsymbol{n}}$ across the ramp.

The observed magnetic and density compression ratios are 3.1 and 3.3, respectively, and we estimated the shock Alfvén Mach number (based on the magnetic overshoot Mellott & Livesey 1987) to lie between 4.5 and 5.1. Based on an upstream density of N_e = 25 cm^{-3}, the corresponding upstream solar wind speed was between 292 and 331 km s^{-1}. It is relevant to note that the value of electron density quoted here is measured upstream (around 13:00) in the pristine solar wind and is lower than the value shown in Fig. 3a (∼35 cm^{-3}). The logic behind this is that there was an increase in the spacecraft potential immediately before the shock, which is not followed in the plasma line and is still under investigation. Still, the value of N_e = 25 cm^{-3} is consistent with the solar wind model run that is discussed later. These shock parameters are summarized in Table 1 above.

Table 1. Parameters for the Venus bow shock crossing on 27 December 2020 at 12:40:00.

Parameter	Value
$\mathbf{B}_u$ [nT]	[−3.0, 7.3, 4.0]
$\lvert\mathbf{B}_d\rvert$ / $\lvert\mathbf{B}_u\rvert$	3.12
θ_{bn} [°]	88.6
$\hat{\boldsymbol{n}}$ (model)	[−0.59, 0.15, −0.79]
Shock overshoot (2 Hz, 128 Hz)	(0.38, 0.5)
N_u [cm^{-3}]	25
N_d/N_u	3.32
Alfveń Mach number (M_A)	4.5–5.1
$\lvert\mathbf{V}_u\rvert$ [km s^{-1}]	292–331

Notes. All vectors are expressed in Venus Solar Orbital (VSO) coordinates.

Figure 2 shows the bow shock crossing in shock oriented coordinates, where $\mathbf{t}_1 = \hat{\boldsymbol{n}}$ is along the normal, $\mathbf{t}_2 = \hat{\boldsymbol{n}} \times \mathbf{B}_u / |\hat{\boldsymbol{n}} \times \mathbf{B}_u|$ is perpendicular to the plane containing $\hat{\boldsymbol{n}}$ and $\mathbf{B}_u$, and $\mathbf{t_3} = \mathbf{t_1} \times \mathbf{t_2}$ completes the orthogonal set.

$\mathbf{B_{t1}}$ shown in panel b exhibits a negligible offset from upstream to downstream, which is evidence of an accurate shock normal direction. On the other hand, there were variations in $\mathbf{B} \cdot \hat{\boldsymbol{n}}$ of around 8 nT. This signifies the presence of embedded structures that have normal directions different to $\hat{\boldsymbol{n}}$ or are indicative of localized variations of the shock surface. The variations in $\mathbf{B_{t1}}$ also appear in the $\mathbf{B_{t2,t3}}$ but have significantly higher amplitudes. Along the $\mathbf{t_3}$ direction, shown in panel d, the amplitudes of these structures are surprisingly similar to the shock amplitude and result in a highly complex magnetic shock profile.

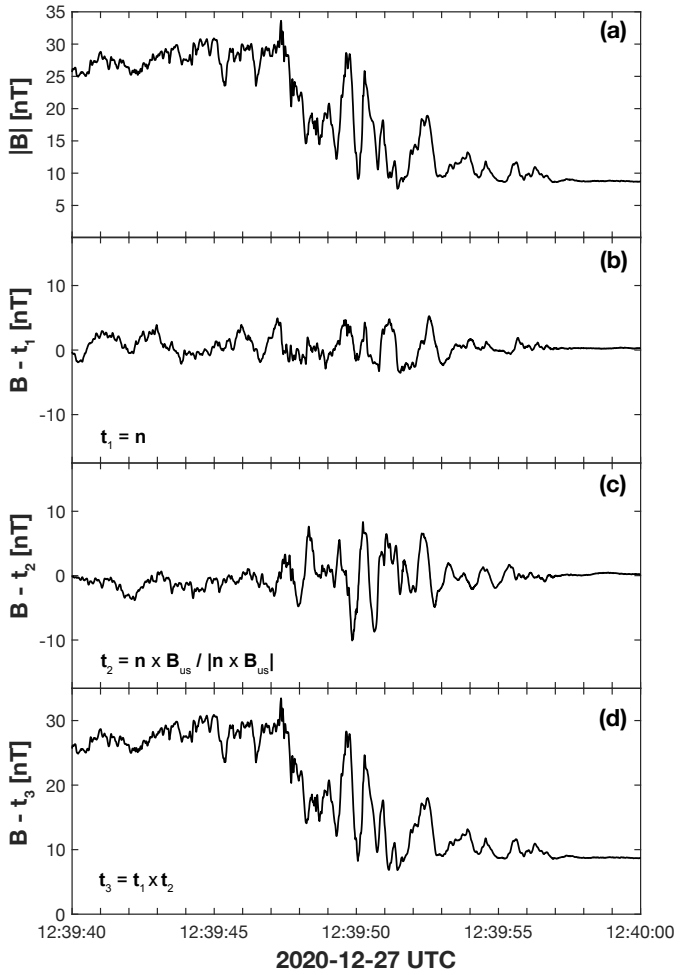

Fig. 2. Magnetic field profile of the Venus bow shock crossing in shock oriented coordinates. *Panel a*: magnetic modulus whereas *panels b–d*: $\mathbf{t}_{1,2,3}$ components. Along $\mathbf{t}$, a negligible offset and variation is suggesting a reliable $\hat{\boldsymbol{n}}$.

The direct calculation of the shock Alfvén Mach number was not possible because measurements of the in situ plasma conditions were unavailable. Nevertheless, a linear relationship between the magnetic overshoot in quasi-perpendicular shocks and M_A was reported by Mellott & Livesey (1987). These results apply to this study since we observed a distinct magnetic overshoot, consistent with supercritical quasi-perpendicular shocks. In this context, the shock overshoot (O) is defined as

$$O = (B_m - B_d)/B_d, \quad (1)$$

where B_m is the maximum field across the shock and B_d is the average downstream magnetic field. According to Mellott & Livesey (1987), small scale variations may provide larger values of B_m, so we provided overshoot values for **B** filtered to 2 Hz and the unfiltered 128 Hz to provide an estimate of the possible limits. Thus, we removed the higher frequency components to determine a lower limit on O. From Fig. 2 in Mellott & Livesey (1987), we estimated that M_A is between 4.5 and 5.1 based on the time series at 2 Hz and 128 Hz, respectively.

From M_A, we attempted to estimate the upstream solar wind speed using

$$M_A = \mathbf{V}_{sw} \cdot \hat{\boldsymbol{n}}/V_A, \quad (2)$$

where V_A is the Alfvén speed $V_A = |\mathbf{B}|/\sqrt{N_p \mu_0 m_p}$. Assuming a purely radial solar wind flow (i.e., $\hat{\boldsymbol{V}}_{\mathbf{sw}} = [-1, 0, 0]$) and $N_p \approx N_e$, the upstream solar wind speed along the radial direction can be estimated from

$$V_x = \frac{\mathbf{V}_{sw} \cdot \hat{\boldsymbol{n}}}{\cos(\theta_{Vn})}, \quad (3)$$

where θ_{Vn} is the angle between $\hat{V}x$ and $\hat{\boldsymbol{n}}$. The $\mathbf{V}_{sw} \cdot \hat{\boldsymbol{n}}$ term is evaluated from Eq. (2) since V_A is known and M_A is estimated from O (Eq. (1)). Although the Mellott & Livesey (1987) empirical relationship did not assume a pure radial solar wind flow, this should be the case in most circumstances. Based on the above, we estimated V_x to be between 292 and 331 km s^{-1}.

To verify our estimation of the solar wind speed, we modeled the solar wind with the European heliospheric forecasting information asset (EUHFORIA) (Pomoell & Poedts 2018), available for users from the European Space Agency (ESA) Space Situational Awareness Portal[1]. EUHFORIA consists of two parts: a large scale coronal field model from the photosphere up to 0.1 AU and data-driven solar wind plasma parameters, which are then used as boundary conditions to drive a 3D MHD model of the inner heliosphere up to 2 AU. From the model run (not shown), it is apparent that Venus and SolO were immersed in a relatively slow solar wind stream. According to these results, the solar wind speed and density were around 300 km s^{-1} and density 25 cm^{-3}, respectively. The model solar wind speed lied within the range of the above calculation and the density was around what we expected from our measurements in the pristine solar wind, therefore this vindicated our estimate of M_A. However, this comparison was only valid for the large scale comparison of the solar wind and did not rule out the possibility of local variations in solar wind properties at Venus.

3.2. Analysis of shock substructures

Plotted in Fig. 3 are N_e, $|\mathbf{B}|$, B_{xyz} and a wavelet coherency spectrum for N_e and $|\mathbf{B}|$. The arrows in panel d indicate the phase according to a unit circle where directions pointing to the right side correspond to content that is in phase. To compute the coherency spectra, N_e was resampled to match the sampling resolution of the magnetic field.

In both magnetic field and density, the shock transition exhibits highly non-laminar behavior by the manifestation of complex multiscale structures across varying amplitudes. Interestingly, the large amplitude magnetic shock substructures already mentioned and shown in panel b were also visible in the electron density observations. This is most prominently demonstrated within the highlighted regions labeled (1–3). According to the coherency spectra, the density and magnetic structures are coherent and in-phase. In both cases, the amplitude of these structures was significant compared to the relative change in each quantity from upstream to downstream. Each structure was also approximately the same period of around 0.7 s (Δt). A summary of the properties of these structures is listed in Table 2.

We performed MVA analysis on the magnetic field during each of the three substructures to determine the local shock normal ($\hat{\boldsymbol{n}}_{loc}$). By local shock normal, we refer to the normal directions of the substructures, which differs from the global shock surface normal calculated using the model normal and minimum variance of the ramp. The local shock normal directions are listed in Table 2 together with the eigenvalue ratio λ_2/λ_3, which is a measure of confidence in the $\hat{\boldsymbol{n}}_{loc}$ direction. The statistical error on the eigenvector pairings were also computed (see Paschmann & Daly 1998 and Khrabrov & Sonnerup 1998)

[1] http://swe.ssa.esa.int

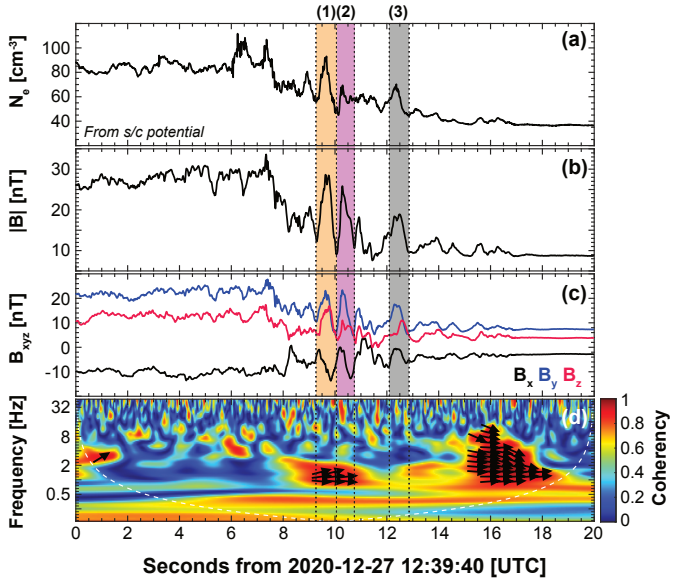

Fig. 3. Shock substructure in density and magnetic field. *Panels a and b*: electron density determined from the spacecraft potential and the magnetic field modulus. A wavelet coherency spectrum is shown in *panel c*, which demonstrates that *panels a and b* share common variations around 0.5–1 Hz during the shock front, which are in phase. Highlighted in orange, purple, and gray are the shock substructures, which are discussed in the text.

and are listed as the parameter $\Delta\theta_{ij}$, where subscripts i and j indicate the individual eigenvectors considered for each error estimate. It is evident that the angular error on each local shock normal estimate is negligible and should not play a role in any further interpretation. We also computed $\hat{\boldsymbol{n}}_{\rm loc}$ using shorter nested regions within each structure and the directions remained unchanged, thus these vectors appear to be robust and reliable. The values of λ_2/λ_3 for the first two structures were over the generally accepted threshold of 10; however, this was below 10 for the third structure. Nevertheless, smaller nested MVA analysis provided the same angles and $\lambda_2/\lambda_3 \gg 10$, and the angular error remained small. Thus, evidence suggested that this direction was reliable. Using $\hat{\boldsymbol{n}}_{\rm loc}$, we calculated $\theta_{n_{\rm mod\text{-}loc}}$, which is the angle between the global shock surface normal (from the model) and the local normal directions at the structures. The value of $\theta_{n_{\rm mod\text{-}loc}}$ indicates the degree to which the local normal varies with respect to the global shock normal. Hodograms across the interval bounded by structures one and two (orange and purple regions) are shown in Fig. 4, indicating that these substructures are circularly left-hand polarized in the spacecraft frame. The minimum variance direction is well defined since $\lambda_2/\lambda_3 \sim 15$. Before computing the hodograms, the data were band-pass filtered between 0.5 Hz and 3 Hz since the structures are both around 1.4 Hz.

The amplitude of the structures are listed in Table 2 as ΔB and ΔN_e. These quantities were computed by first high-pass filtering (>0.5 Hz) the data to remove the background trend, and then evaluating the peak value within the highlighted regions for N_e and $|\mathbf{B}|$. Surprisingly, ΔB for structure 1 and structure 2 exceed 14 nT, which exceeds the local background magnetic field (~12 nT) and is comparable to the change in $|B|$ from upstream to downstream. Although ΔB is smaller for structure 3 (8 nT), it can still be considered comparable to the background magnetic field (~10 nT). A similar scenario arises for ΔN_e in the sense that the values are comparable to the background value and shock amplitude.

Table 2. Parameters of the three shock substructures highlighted in Fig. 3.

Parameter	Structure 1	Structure 2	Structure 3
Time	12:39:49.30	12:39:50.06	12:39:52.08
ΔT (s)	0.77	0.70	0.79
ΔB (nT)	14.98	14.30	8.01
ΔN_e (cm^{-3})	31.97	22.90	13.41
$\hat{\boldsymbol{n}}_{\rm loc}$	[0.58, −0.41, 0.70]	[0.43, −0.37, 0.82]	[0.88, −0.47, −0.08]
λ_2/λ_3	58.7	20.4	6.6
$\theta_{n_{\rm mod\text{-}loc}}$ (°)	15.97	15.60	57.95
$\Delta\theta_{32}$ (°)	0.77	1.42	2.62
$\Delta\theta_{31}$ (°)	0.54	0.71	1.09
$\Delta\theta_{21}$ (°)	1.27	1.08	1.47

Notes. The angles $\Delta\theta_{i,j}$ provide the statistical angular error between eigenvectors i and j using Eq. (8.23) in Paschmann & Daly (1998) and discussed in detail by Khrabrov & Sonnerup (1998).

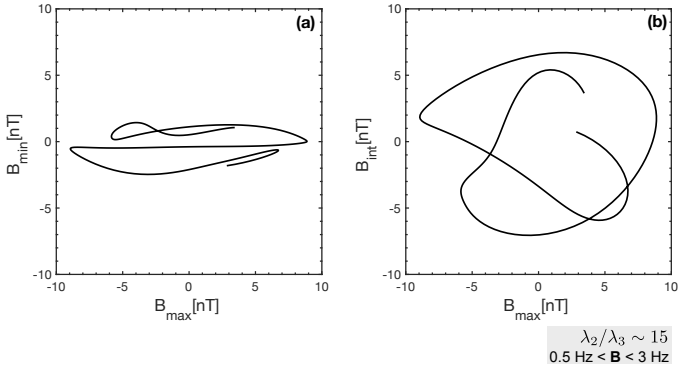

Fig. 4. Hodograms over the interval bounded by structures one and two shown in Fig. 3. The data were band-pass filtered between 0.5 Hz and 3 Hz prior to computing the hodogram.

Important unit vector directions are plotted in Fig. 5, which are in the $\mathbf{t}_{1,2,3}$ shock frame. The black and red arrows correspond to $\hat{\boldsymbol{n}}$ (along $\mathbf{t}_1$) and $\mathbf{B}_u$, respectively. The dark blue, green, and light blue arrows show the directions of each structure (i.e., $\hat{\boldsymbol{n}}_{\rm loc}$). The purple arrow indicates the spacecraft trajectory at the time of the shock crossing.

The first two substructures are well-aligned with the shock normal direction (~16°) and show no explicit preference in the $\mathbf{t}_2$ or $\mathbf{t}_3$ directions. The third substructure is increasingly oblique and shows a preference for the coplanarity plane. What is also apparent here is that the spacecraft trajectory is oblique (~56°) to the shock normal as evident in Fig. 1. Also, the spacecraft trajectory is highly oblique to the structures 1–3 (59°, 67°, 36°). A caveat to interpreting these directions is the shock speed, which on occasions can far exceed the spacecraft speed and importantly can oscillate around the spacecraft position. Still, we see no indication of multiple shock crossings, solar wind discontinuities, or unusually high solar wind speeds that would suggest any back-and-forth shock behavior. Later we offer physical explanations for these substructures that take into account these multiple pieces of evidence (angle, polarization properties, amplitude, coherency with density, and the Mach number of the shock) by considering the relevant theoretical explanations and what has been reported at similar Mach number shocks in the literature.

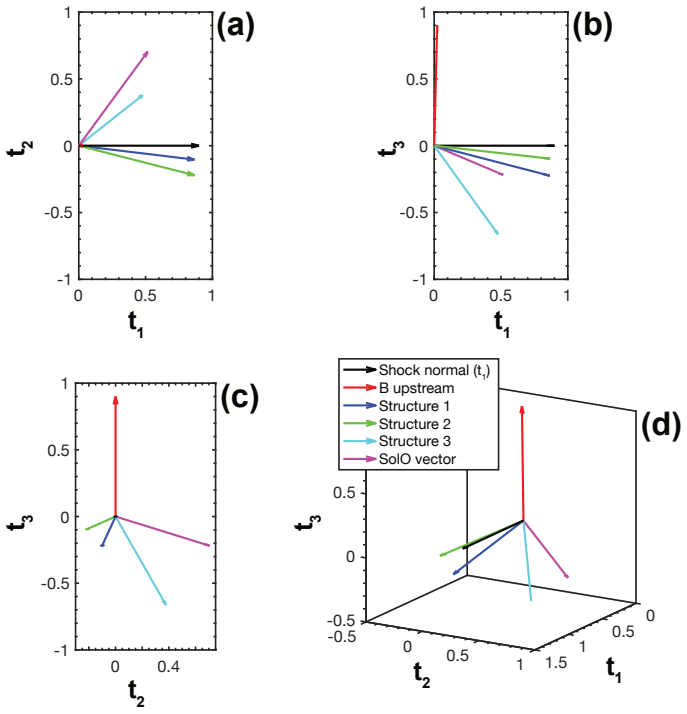

Fig. 5. Key unit vectors in shock coordinates. The black and red arrows represent the shock normal and upstream magnetic field directions, respectively. The purple arrow marks the direction of the spacecraft trajectory at the time of the shock crossing. Indicated by the dark blue, green, and light blue arrows are the directions of the three structures highlighted in Fig. 3, according to minimum variance analysis.

3.3. Characterization of electromagnetic waves

In addition to the lower-frequency substructures, this shock crossing also displayed higher frequency wave-activity throughout the shock front. Figure 6 shows the polarization analysis of the waves using singular value decomposition (Santolík et al. 2003; Taubenschuss & Santolík 2019).

For reference, panel a depicts the magnetic field in VSO coordinates, whereas panels b–d display the SCM magnetic field band-pass filtered between 30 and 120 Hz, electric field, and electron density, respectively. Since E_x was not measured, we define $E_\parallel$ and $E_\perp$ in panel c as the components of E along and perpendicular to the magnetic field in the YZ plane. Wavelet spectrograms of the AC electric field e and the magnetic field from the SCM f are also included. The remaining panels f–j provide a more detailed characterization of the fluctuations in terms of the degree of polarization (DOP), planarity, ellipticity, angle between the wave normal vector direction and the local magnetic field (θ_{kb}), and the Poynting flux. The solid line in panels e–k marks the lower hybrid frequency.

Throughout the shock, these waves are right-handed and circularly polarized (ellipticity ~1) and the degree of polarization remains close to unity. Based on the right-hand polarization throughout the interval and frequencies below the local electron cyclotron frequency, we identify these waves as whistler-mode waves. Between 12:39:55.5 and 57, the wave vector normal direction is rather oblique to the background magnetic field and $\theta_{kb} \sim 45°$. In contrast, before 12:39:54.5, θ_{kb} is significantly more field-aligned and is <10°. Therefore, changes in the wave properties across the shock are observed. It is also worth noting that the oblique waves appear somewhat separated from their field-aligned counterparts as mentioned above. This is evident in the time series data plotted in panel b and the spectrogram in panel f by the clear isolated spectral power around 30 Hz after 12:39:55.5. There are also differences in the Poynting flux plotted in panel j, which indicates that the directional energy flux is along the magnetic field direction ($S_\parallel/|S| \sim 1$), whereas this is substantially more disturbed deeper moving into the shock front, possibly indicating a source region for these waves.

Close to the downstream edge (12:39:46–47.5), there are large amplitude $E_\parallel$ fluctuations exceeding 40 mV m^{-1}, which according to panel e, reach the Nyqvist frequency of 128 Hz. Large field-aligned electric fields with comparable amplitudes to this have been reported at the terrestrial bow shock before (Goodrich et al. 2018) and were also observed just downstream of the Venus shock by Parker Solar Probe (Malaspina et al. 2020). They were attributed to plasma double layers and electron phase space holes that are expected in unstable plasma such as downstream of collisionless shocks. Although these shock geometries were more oblique than the one studied here, Bale et al. (1998) also reported evidence of phase-space holes in quasi-perpendicular shocks close to the downstream overshoot. A caveat here is that the typical time-scales of these structures reported in the literature are on the order of one to a few milliseconds, which is higher than the frequencies we consider. The investigation of these structures is difficult here due to the lack of plasma measurements and although we did not pursue this any further, it should be considered when analyzing future SolO Venus flybys.

4. Discussion

In this section, we provide physical interpretations of these measurements and place our results into context with that reported in the existing literature. The most widely studied bow shock is that at Earth, which has been investigated for decades using multipoint and high-resolution plasma and field observations. The terrestrial bow shock provides an ideal opportunity to compare to this Venus shock crossing since the Earth bow shock occupies a similar Mach number regime to the present case (e.g., Dimmock et al. 2012). The terrestrial bow shock is also the shock where measurements are cable of resolving the relevant shock front behavior while capturing the particle dynamics. These similarities provide valuable insights when interpreting single point measurements in the absence of plasma observations. Such comparisons also offer new understanding on the differences between bow shocks at magnetized and non-magnetized bodies. One notable difference between Venus and Earth is the relative proximity to the ionosphere. However, we do not expect the dynamics of the Venus ionosphere to be important as they would likely occur on significantly longer timescales than those that we consider in this study (1–100 Hz).

The observed quasi-periodic magnetic wave structures can be partially explained by shock ripples (Lowe & Burgess 2003; Johlander et al. 2016, 2018). As a spacecraft encounters multiple ripples along the shock front, it will undergo upstream-downstream-upstream transitions which manifest as magnetic field and density variations, comparable to that observed in this study. In the magnetic field, they seem wave-like and are believed to propagate along the shock surface with $\theta_{kb} \sim 40°$ (Johlander et al. 2018). Furthermore, they are linearly polarized in the coplanarity plane at frequencies nearly three times the upstream ion gyrofrequency (f_{ci}). The Alfvén Mach number of the rippled shocks examined using MMS (see Johlander et al. 2016 and Johlander et al. 2018) was between 6.2 and 7, larger than the first critical Mach number, which is typically around

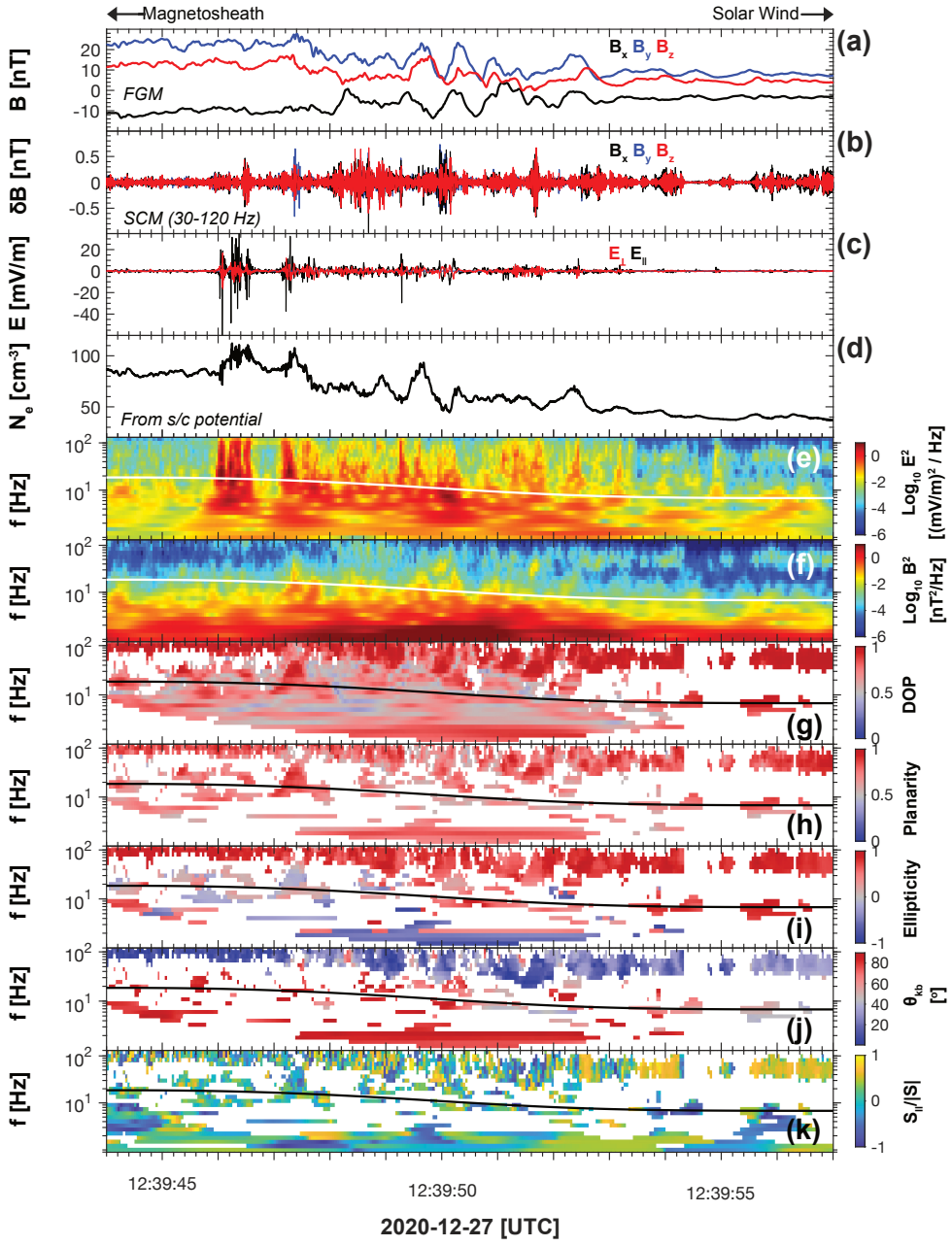

Fig. 6. Polarization analysis of the magnetic and electric field across the shock front. Displayed in *panels a–d* are FGM magnetic field, SCM magnetic field (30–12 Hz), electric field, and electron density, respectively. *Panels e and f* are spectrograms of the electric field and SCM data. The remaining *panels g and h* correspond to the degree of polarization, planarity, ellipticity, θ_{kb}, and Poynting flux.

3. Additionally, the geometries of these shocks were 64°–83°. The shock crossing in this study is also supercritical (M_A ~ 4.5–5.1) with θ_{bn} ~ 89, therefore the shock is in a comparable regime where we would expect ripples to develop based on the aforementioned previous experimental studies. In our study, f_{ci} = 0.13 Hz, which would result in an expected ripple frequency of 0.4 Hz, equivalent to around 2.5 s, longer than the ~0.7 s that we measure. Based on MVA, the local shock normal directions were 16° and 59°, compared to the reported 40°. On the other hand, Kajdič et al. (2019) analyzed irregular ion scale structures at interplanetary shocks and propose a complex shock surface revealing highly varying local shock normal directions. This signifies that interpreting local normal shock directions and the time scale of ripples based on local observations is challenging due to the expected dependence on the scale of the individual structure and the geometry of the encounter. This could contribute to some explanation for the particularly diverging local normal directions (16° and 59°) that we measured. It is also worth noting that MVA indicated that these structures are elliptically polarized, which is not consistent with the MVA polarization reported by Johlander et al. (2018). Hence, although some aspects of these observations are consistent with ripples, there are also inconsistencies. Quantifying the statistical properties of shock ripples will be essential to interpreting single spacecraft measurements such as these. Moreover, this remains an interesting question to shock physics considering ripples may be important to shock dynamics by moderating particle reflection (Johlander et al. 2016, 2018).

Whistler precursors with amplitudes larger than the background field and shock amplitude have also been reported within quasi-perpendicular shocks (Wilson 2012, 2017) due to shock macro-dynamics (e.g., steepening of the shock front) or instabilities. We should point out that the structures we observe have attributes similar to magnetosonic-whistler waves, and consequently this could offer a physical explanation for these measurements. We observe structures that are circularly polarized

(see Fig. 4) and span frequencies from approximately 1 Hz to several Hz, which is consistent with the characteristics of whistler waves described in the literature. Although frequencies less than 3 Hz in the SCM data are influenced by noise, it can be pointed out that the low frequency left-handed and elliptically polarized waves displayed in Fig. 6i are consistent with the MVA analysis. The angle between wave vector normal angle and the shock normal (θ_{kn}) for these waves is also in the range of what is expected for whistler waves in this frequency range, but θ_{kn} can also change significantly. For example, the majority of events analyzed by Wilson (2017) exhibited $\theta_{kn} > 30°$, which is greater than two of our three events (~16°) but consistent with the third (58°). Nevertheless, a small, but a non-trivial portion of the events considered by Wilson (2017) exhibited $\theta_{kn} < 20°$, so this cannot be ruled out.

A key piece of evidence to explain these structures is the small θ_{kn} for two of the structures and small time scale of <1 s, which are consistent with structures expected to be generated in the shock ramp above the whistler critical Mach number (M_w) (Dimmock et al. 2019; Krasnoselskikh et al. 2002) for quasi-perpendicular shocks. The Mach number of this shock is considerably above the expected M_w and the nonlinear critical Mach number (M_{nw}). When $M_w < M_A < M_{nw}$, whistler waves are not able to phase stand upstream and whistler structures can be located inside the shock ramp (Krasnoselskikh et al. 2002; Dimmock et al. 2019), which is consistent with the absence of an upstream wave train and the appearance of substructures within the ramp that we observed. In such cases, whistler structures can develop inside the shock front as a sign of over steepening and nonstationarity, ultimately leading to reformation via a gradient catastrophe. Since $M_A > M_{nw}$ then we would expect this shock to be nonstationary since M_{nw} is the threshold when a gradient catastrophe should occur. Yet, in the absence of plasma measurements, DC electric field, and multipoint observations, this cannot be directly confirmed. It should also be noted that the third structure closer to the ramp is significantly more oblique to the shock normal, which would not be expected from the gradient catastrophe model and is more consistent with a conventional oblique whistler precursor. In addition to regulating the shock front magnetic profile, the structures we observed inside the shock front are expected to play a role in nonadiabatic electron heating due to electric field "spikes" that are associated with this process (Dimmock et al. 2019) and previously reported at quasi-perpendicular shocks (Walker et al. 2004). Unfortunately, the RPW instrument was not configured to measure DC during this shock crossing but will be examined in prospective SolO flybys where the Venus bow shock will continue to be analyzed in detail.

The supercritical nature of this shock allows us to rule out ion sound subshocks (Kennel et al. 1985) as an explanation, which are relevant to energy dissipation between the first and second critical Mach numbers. In addition, the highly perpendicular geometry enables the elimination of any impacts from foreshock structures as they are only applicable to quasi-parallel shocks (Kennel et al. 1985). However, it is necessary to keep in mind that the physical explanation for these observations can change if the shock parameter regime is different from the case presented here. The time stationary behavior of the shock itself could also be an explanation if we consider a planar shock moving back and forth over the spacecraft. However, for this scenario, it would be presumed that on these second timescales, the global shock normal would be consistent with the normal directions of the structures themselves, which is not the case here. In addition, the difference in the amplitudes and profiles of the magnetic field and density measurement for the structures does not point to this situation. As a result, there is considerably stronger evidence to support the physical interpretations outlined above.

Higher frequency (30–120 Hz) waves were prevalent throughout the shock crossing and based on their characteristics (polarization, direction, frequency), we classify them as whistler waves. There was definite evolution in the propagation angle; closer to the shock foot the waves were oblique, whereas deeper into the foot they shifted to more field-aligned. Oblique θ_{kb} and field-aligned Poynting flux directed away from the shock such as the wave packets close to the foot are consistent with the growth due to electron beam instabilities (Tokar et al. 1984) from electrons that are reflected from the shock front.

The evolution of the waves to more field-aligned θ_{kb} could be explained by these waves being generated by temperature anisotropies ($T_\perp > T_\parallel$) in the shock (Hull et al. 2012). This would also be consistent with the upstream wave packets appearing more isolated (see Fig. 6). The highly varying Poynting flux could be evidence that the spacecraft traversing the source region for these waves, which is likely a region of high temperature anisotropy. This result implies complex circumstances in the sense that wave generation within the shock can take place due to multiple mechanisms. This could be an explanation for the excitation of waves that exhibit changing features. On the other hand, the Poynting flux may be challenging to determine in the ramp owing to the appearance of complex magnetic structures and the broadband electrostatic turbulence overlapping with the frequency of interest. Therefore, this cannot be ruled out as an explanation for the changing Poynting flux and the shift of θ_{kb}. It is also worth considering that even higher frequency (up to 10 kHz) electrostatic fluctuations are observed across the shock (Hadid et al. 2021), but a temporal association between them and the lower frequency variations is not feasible in this study. Nevertheless, lower frequency (1–10 Hz) whistler waves have been proposed to be connected to higher frequency whistler waves by the generation of currents and local temperature anisotropies (Hull et al. 2020).

The observations by SolO during the outbound crossing of the Venus bow shock during its first gravity assist maneuver showed intriguing magnetic and density structures embedded across the shock layer. These high cadence measurements demonstrate that the Venus bow shock is extremely structured across various scales, presenting many features similar to those reported at the terrestrial bow shock using multipoint measurements. The large amplitude structures exhibit some features consistent with shock rippling (Johlander et al. 2016, 2018) but then again, some characteristics of our measurements are similar to whistler waves (Wilson 2017; Dimmock et al. 2019). To date, no large scale statistical study of shock rippling has been conducted, and as a result, the properties of ripples as a function of the many shock parameters remain unclear. Statistical studies of whistler waves in the shock have been conducted (Wilson 2017) but show a variety of wave attributes, such as propagation angles and time scales. Also, the first direct observation of whistler substructures as confirmation of the gradient catastrophe model (Dimmock et al. 2019) was only recently reported. It will be necessary to disentangle these diverse multiscale shock substructures and classify the physical mechanisms responsible for various shock regimes. Although multipoint measurements such as MMS are expected to shed more light on this topic, it will also be essential to continue investigating related structures across various shock environments (e.g., interplanetary and non-terrestrial bow shocks), for which Solar Orbiter will provide more opportunities. Importantly, this study highlights the

necessity to differentiate between shock nonstationarity, rippling, and wave structures. This will be essential to interpreting single spacecraft planetary bow shock observations for missions that are now launched such as BepiColombo and also upcoming missions such as JUICE. Further SolO gravity assists in the following years will afford new opportunities for the Venus bow shock to be measured and analyzed in more comprehensive detail.

5. Conclusions

From our analysis we can draw the following key conclusions:

1. Solar Orbiter observed a highly structured Venusian bow shock with multiple large amplitude magnetic and density structures comparable to the shock amplitude in concert with higher frequency waves.
2. The shock-substructures show many similarities to large amplitude whistler waves, which can be emitted by the shock ramp or be generated from instabilities.
3. Another explanation for shock front substructures are spatial variations on the shock surface known as ripples and this will become more apparent in forthcoming studies when the statistical characteristics of ripples are soundly established.
4. The shock substructures occur in concert with higher frequency whistler waves over the shock front between 30 and 120 Hz.
5. There is no clear temporal association between the lower frequency substructures and higher frequency whistler waves.
6. Higher frequency whistler waves show interesting evolution across the shock front in terms of frequency and angle to the background magnetic field. This may be indicative of varying generation mechanisms within the shock (e.g., electron beams and temperature anisotropy) or due to interference from complex magnetic structures and electrostatic turbulence.

To conclude, this study highlights the complicated multiscale physics of collisionless shocks and the unresolved questions concerning rippling, nonstationarity, and waves that are often reported across various plasma environments. Collisionless shocks continue to be an essential science goal for Solar Orbiter, and the Venus bow shock will perform a substantial role as it is investigated in future gravity assists while the mission proceeds to characterize interplanetary shocks over the inner-heliosphere.

Acknowledgements. APD and EY were funded by the Swedish Civil Contingencies Agency grant 2016-2102. APD received financial support from the Swedish National Space Agency (Grant #2020-00111) and the EU Horizon 2020 project SHARP: SHocks: structure, AcceleRation, dissiPation # 101004131. EY would like to acknowledge the Swedish National Space Agency Grants #86/20 and #145/18. RCA is supported under NASA contract NNN06AA01C. Solar Orbiter magnetometer operations are funded by the UK Space Agency (grant ST/T001062/1). Tim Horbury is supported by STFC grant ST/S000364/1.

References

Allen, R. C., Cernuda, I., Pacheco, D., et al. 2021, A&A, 656, A7
Bale, S. D., Kellogg, P. J., Larsen, D. E., et al. 1998, Geophys. Res. Lett., 25, 2929
Bale, S. D., Balikhin, M. A., Horbury, T. S., et al. 2005, in Quasi-perpendicular Shock Structure and Processes, eds. G. Paschmann, S. J. Schwartz, C. P. Escoubet, S. Haaland, et al. (Dordrecht: Springer), 161
Balikhin, M. A., de Wit, T. D., Alleyne, H. S. C. K., et al. 1997, Geophys. Res. Lett., 24, 787
Dimmock, A. P., Balikhin, M. A., Krasnoselskikh, V. V., et al. 2012, J. Geophys. Res.: Space Phys., 117, A02210
Dimmock, A. P., Balikhin, M. A., Walker, S. N., & Pope, S. A. 2013, Ann. Geophys., 31, 1387
Dimmock, A. P., Russell, C. T., Sagdeev, R. Z., et al. 2019, Sci. Adv., 5, eaau9926
Fairfield, D. H. 1974, J. Geophys. Res., 79, 1368
Goodrich, K. A., Ergun, R., Schwartz, S. J., et al. 2018, J. Geophys. Res.: Space Phys., 123, 9430
Hadid, L. Z., Edberg, N. J. T., Chust, T., et al. 2021, A&A, 656, A18
Horbury, T. S., OBrien, H., Carrasco Blazquez, I., et al. 2020, A&A, 642, A9
Hull, A. J., Muschietti, L., Oka, M., et al. 2012, J. Geophys. Res.: Space Phys., 117, A12104
Hull, A. J., Muschietti, L., Le Contel, O., Dorelli, J. C., & Lindqvist, P.-A. 2020, J. Geophys. Res.: Space Phys., 125, e2019JA027290
Jannet, G., Dudok de Wit, T., Krasnoselskikh, V., et al. 2021, J. Geophys. Res.: Space Phys., 126, e2020JA028543
Johlander, A., Schwartz, S. J., Vaivads, A., et al. 2016, Phys. Rev. Lett., 117, 165101
Johlander, A., Vaivads, A., Khotyaintsev, Y. V., et al. 2018, Plasma Phys. Control. Fusion, 60, 125006
Kajdič, P., Preisser, L., Blanco-Cano, X., Burgess, D., & Trotta, D. 2019, ApJ, 874, L13
Kennel, C. F., Edmiston, J. P., & Hada, T. 1985, Am. Geophys. Union Geophys. Monograph Ser., 34, 1
Khotyaintsev, Y. V., Graham, D. B., Vaivads, A., et al. 2021, A&A, 656, A19
Khrabrov, A. V., & Sonnerup, B. U. Ö. 1998, J. Geophys. Res., 103, 6641
Krasnoselskikh, V. 1985, Sov. Phys. Jetp, 62, 282
Krasnoselskikh, V. V., Lembège, B., Savoini, P., & Lobzin, V. V. 2002, Phys. Plasmas, 9, 1192
Lobzin, V. V., Krasnoselskikh, V. V., Musatenko, K., & Dudok de Wit, T. 2008, Ann. Geophys., 26, 2899
Lowe, R. E., & Burgess, D. 2003, Ann. Geophys., 21, 671
Luhmann, J. G. 1986, Space Sci. Rev., 44, 241
Maksimovic, M., Bale, S. D., Chust, T., et al. 2020, A&A, 642, A12
Malaspina, D. M., Goodrich, K., Livi, R., et al. 2020, Geophys. Res. Lett., 47, e2020GL090115
Martinecz, C., Boesswetter, A., Fränz, M., et al. 2009, J. Geophys. Res.: Planets, 114, E00B30
Mellott, M. M., & Livesey, W. A. 1987, J. Geophys. Res.: Space Phys., 92, 13661
Morse, D. L., Destler, W. W., & Auer, P. L. 1972, Phys. Rev. Lett., 28, 13
Müller, D., St. Cyr, O. C., Zouganelis, I., et al. 2020, A&A, 642, A1
Ofman, L., & Gedalin, M. 2013, J. Geophys. Res.: Space Phys., 118, 5999
Owen, C. J., Bruno, R., Livi, S., et al. 2020, A&A, 642, A16
Paschmann, G., & Daly, P. W. 1998, ISSI Scientific Reports Series 1
Phillips, J. L., & Russell, C. T. 1987, J. Geophys. Res.: Space Phys., 92, 2253
Pitňa, A., Šafrànkovà, J., Němeček, Z., Ďurovcovà, T., & Kis, A. 2021, Front. Phys., 8
Pomoell, J., & Poedts, S. 2018, J. Space Weather Space Clim., 8, A35
Rodríguez-Pacheco, J., Wimmer-Schweingruber, R. F., Mason, G. M., et al. 2020, A&A, 642, A7
Russell, C. 2007, J. Atmos. Solar-Terrest. Phys., 69, 1739
Santolík, O., Parrot, M., & Lefeuvre, F. 2003, Radio Sci., 38
Sulaiman, A. H., Masters, A., Dougherty, M. K., et al. 2015, Phys. Rev. Lett., 115, 125001
Sundberg, T., Boardsen, S. A., Slavin, J. A., et al. 2013, J. Geophys. Res.: Space Phys., 118, 6457
Taubenschuss, U., & Santolík, O. 2019, Surveys Geophys., 40, 39
Tokar, R., Gurnett, D., & Feldman, W. 1984, J. Geophys. Res.: Space Phys., 89, 105
Volwerk, M., Horbury, T. S., Woodham, L. D., et al. 2021, A&A, 656, A11
Walker, S. N., Alleyne, H. S. C. K., Balikhin, M. A., André, M., & Horbury, T. S. 2004, Ann. Geophys., 22, 2291
Wilson, L. B. I., Koval, A., Szabo, A., et al. 2012, Geophys. Res. Lett., 39, L08109
Wilson, L. B. I., Koval, A., Szabo, A., et al. 2017, J. Geophys. Res. (Space Phys.), 122, 9115
Wimmer-Schweingruber, R. F., Pacheco, D., Janitzek, N., & Espinosa Lara, F. 2021, A&A, 656, A22
Winske, D., & Quest, K. B. 1988, J. Geophys. Res.: Space Phys., 93, 9681
Wu, C. S., Winske, D., Tanaka, M., et al. 1984, Space Sci. Rev., 37, 63
Yuan, X., Cairns, I. H., Trichtchenko, L., Rankin, R., & Danskin, D. W. 2009, Geophys. Res. Lett., 36
Zank, G. P., Nakanotani, M., Zhao, L. L., et al. 2021, ApJ, 913, 127
Zhang, Y., Matsumoto, H., Kojima, H., & Omura, Y. 1999, J. Geophys. Res.: Space Phys., 104, 449